PROCEEDINGS, 50th Workshop on Geothermal Reservoir Engineering
Stanford University, Stanford, California, February 10-12, 2025
SGP-TR-229

Alkali-activated Aluminate-based Cement for Use in Supercritical Geothermal Wells

Michelle Devoe[1], Sizhan Liu[1], Tatiana Pyatina[1], Toshifumi Sugama[1], Jianming Bai[2]

1) Interdisciplinary Science Department, Brookhaven National Lab, Upton NY 11973

2) National Synchrotron Light Source II, Brookhaven National Lab, Upton NY 11973

tpyatina@bnl.gov

Keywords: clinker-free, cement, composite, supercritical, well development

ABSTRACT

Supercritical geothermal wells, capable of producing ten times more energy than low temperature EGS wells, offer a solution to the increasing energy demand in the United States. Most supercritical wells developed to date have failed and none currently supply energy to the grid because the materials used in well development fail under supercritical conditions, including Portland Cement which degrades quickly due in part to decalcification. In this study, an alkali-activated aluminate-based composite is tested for its suitability in supercritical geothermal wells. The composite is hydrothermally cured for 1 day at 300°C, 1 day at 400°C, and 7 days at 400°C. The mechanical properties of each composite are measured, and the composition and microstructure is determined using FTIR, XRD, and SEM-EDS. Compressive strength, Young's modulus, and toughness increase with increasing temperature and exposure duration, which coincides with the transformation and ultimate disappearance of zeolites, and the development of paragonite. Overall, the composite cured at each exposure condition exhibits acceptable properties for well development.

1. INTRODUCTION

While 5 terrawatts of potential geothermal energy have been estimated in the United States, accessible with the use of EGS and AGS systems, only 4 GW of geothermal energy is on the grid, provided by conventional geothermal wells (not EGS or AGS) with temperatures of 150-300°C (Reinsch et al. 2017, Blakenship et al. 2024). As power and energy demands increase in the United States, supercritical geothermal wells combined with enhanced geothermal system (EGS) technology offer the potential to increase geothermal energy output tenfold. Compared to low temperature EGS wells (<200°C) which produce at best 5 MWe (megawatts electricity) per well, and a typical shale gas well which produces 10 MWe, supercritical geothermal wells, which are drilled into hot rock with working fluids above the critical point of water (>375°C and 221 bar for pure water), are estimated to produce up to 50 MWe per well (Cladouhos et al. 2018, Petty et al. 2020).

Supercritical drilling projects have been conducted in many countries including Iceland, USA, Japan, Kenya. Most wells have failed for various reasons including cementing failure, and casing damage, corrosion, or collapse, and none are currently producing power (Kruzewski and Wittig 2018, Suryanarayana et al., accessed 2025). Part of the cause of failure in all geothermal wells, not just supercritical wells, is due to the poor durability of common well materials in the hostile geothermal environment. At present, Portland cement and steel casing are most common for a geothermal well construction. However, the well environment can be strongly acidic and result in acid attack and carbonation/decalcification of portlandite and calcium-silicate hydrate phases, leading to cement dissolution and potential failure, as well as compromised casing corrosion protection (Biczok 1967, Gallus et al. 1979, Beddoe & Dorner 2005, Pyatina & Sugama 2016).

Aluminate-based cement is appealing due to its lack of Ca, providing resistance to carbonation, one of the primary causes for degradation of Portland cement in geothermal wells. Two cementitious composites with aluminum-rich components have demonstrated good durability in geothermal environments and have been identified as alternatives to Portland cement for well development. Thermal shock resistant cement (TSRC) made of a calcium aluminate cement/fly ash F (CAC/FAF) blend has demonstrated good acid resistance as well as thermal shock resistance and excellent self-healing properties (Gill et al. 2012, Pyatina & Sugama 2016, Sugama & Pyatina 2019). And a calcium aluminate phosphate/fly ash F (CAP/FAF) blend designed for applications in CO-rich geothermal wells (Sugama & Carciello 1992, 1993, 1995) possessed good strength recovery after damage and bond strength re-adherence between cement and casing following initial debonding (Sugama & Pyatina 2019). Aluminate-cements have shown good durability in high temperature (300-350°C) field exposure tests at the Newberry well site and under supercritical conditions (Pyatina et al. 2024).

The demonstrated success of aluminate-based cement chemistries in geothermal wells encourages further study on the system and raises the question of its suitability for supercritical environments. Boehmite [AlO(OH)], which can be synthesized from gibbsite in highly alkaline solutions (Gong et al. 2003, Earnest et al. 2018, Zhang et al. 2019), was a resultant phase in both TSRC and CAP/FAF, and due to its acid-resistant chemistry, is the primary component of the aluminate-based cement system in this study. In this study, aluminate-based cement made from gibbsite, silica flour, and sodium metasilicate is analyzed following supercritical exposure to evaluate its suitability for supercritical well development.

2. MATERIALS AND METHODS

2.1 Materials

Gibbsite powder [$Al(OH)_3$] (Emplura) with bulk density of 90 g/100 mL and particle size of <150 um for 90% of the material was obtained from Sigma Aldrich (Darmstadt, Germany). Silica flour (SiO_2) with particle size of 40-250 um was obtained from U.S. Silica Corporation (Texas, USA). Alkali activator sodium metasilicate (SMS) powder (Na_2SiO_3) ("MetsoBeads 2048") with 93% purity and particle size distribution from 0.23-0.85 mm and 50.5/46.6 NaO/SiO_2 weight ratio was obtained from PQ Corporation (Pennsylvania, USA).

Figure 1 shows Attenuated Total Reflectance-Fourier Transform Infrared Spectroscopy (ATR-FTIR) spectra in the frequency range from 4000 to 650 cm^{-1} for these stating materials. The spectrum of aluminum hydroxide, $Al(OH)_3$, is that of gibbsite (Tarte 1967, Schroeder 2002). The gibbsite crystalline structure involves octahedral sheets of aluminum hydroxide, where the O-H bond stretching (ν_{O-H}) and bending (δ_{O-H}) vibration modes encompass six stretching frequencies at 3621, 3522, 3434, and 3367 cm^{-1} (ν_{O-H}), and two bending frequencies at 1015 and 963 cm^{-1} (δ_{O-H}). The Al-O bond stretching (ν_{Al-O}) in octahedral AlO_6 groups can be recognized by the presence of 738 cm^{-1} and 661 cm^{-1} bands. For silica flour, all bands were directly related to SiO_2 in SiO_4 (tetrahedral) groups (Fidalgo & Ilharco 2001, Innocenzi et al. 2003, Ramasamy & Suresh 2009); the first two bands at 1084 and 1056 cm^{-1} represent asymmetric stretching ($\nu_{as\ Si-O}$) of Si-O bond and the next two bands at 795 and 775 cm^{-1} belong to symmetric stretching ($\nu_{s\ Si-O}$) of Si-O, while 693 cm^{-1} band is associated with Si-O-Si bending (δ_{O-Si-O}) mode. The bands of the SMS spectrum are attributed as follows; ν_{Si-O} stretching in Si-O-Na bond gives the bands of 1029 and 963 cm^{-1} and ν_{Si-O} in tetrahedral SiO_4 the bands at 892, 875, and 711cm^{-1} (Ferraro & Manghnani 1972, Husung & Doremus 1990, Allahdin et al. 2016, Li et al. 2019). Additionally, the band at 1452 cm^{-1} may be assigned to $\nu_{as\ C-O}$ in CO_3^{2-} group of a carbonate compound like Na_2CO_3 (Xyla & Koutsoukos 1989, Ylmen & Jaglid 2013). Then, 875 cm^{-1} band overlapping with SiO_4, is O-C-O out-of-plane bending (δ_{O-C-O}) in the CO_3^{2-} group.

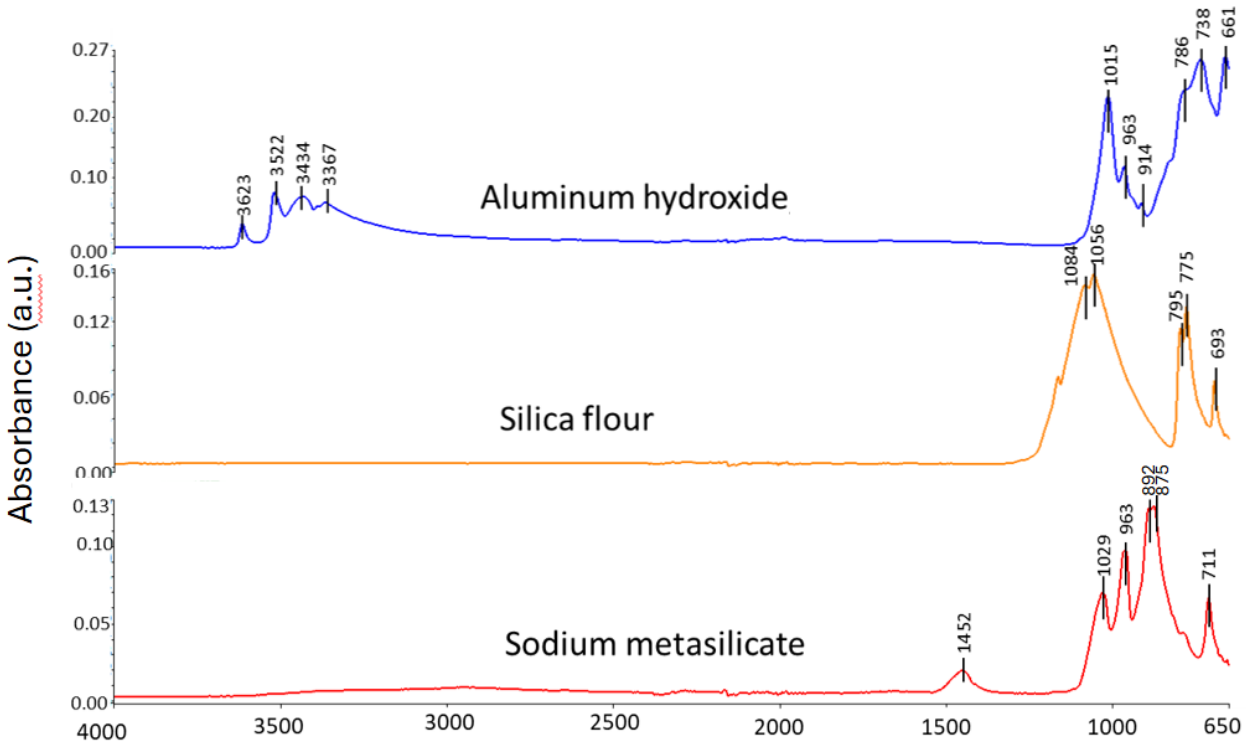

Figure 1. ATR-FTIR spectra of starting materials.

2.2 Sample Preparation

A dry blend of 60 wt% gibbsite and 40 wt% silica was combined with 5% of the total mass of gibbsite and silica as SMS. The water was added to blend at 0.44 water-to-total blend ratio, and the slurry was hand-mixed for 1 minute. The slurry was poured into borosilicate glass tubes (18 mm inner diameter x 150 mm height). Enough slurry was made to produce three 18 mm x 36 mm cylinders for each exposure condition. The tubes were placed in 99±1% relative humidity at 85°C humidity for 24 hours to initiate the alkali-dissolution of gibbsite. The tubes were then transferred to a Parr (Illinois, USA) non-stirred pressure vessel, from hereon referred to as an autoclave, loaded with tap water and set to 300°C for 24 hours. During this process, the cement composite solidified and the borosilicate tubes degraded due to the alkalinity. Following 24 hour exposure, the samples were removed from the autoclave and the solid composite was separated from the degraded borosilicate tubes. The 300°C 1 day samples were removed for testing and characterization, and the remaining

samples were placed back into the autoclave and exposed to supercritical H_2O (scH_2O) conditions of 400°C and 24.1 MPa for 1 and 7 days.

2.3 Measurements

Water-fillable porosity is calculated using $(W_{wet}-W_{dry})/V \times 100$, where W_{wet} is the weight of water-saturated sample and W_{dry} is the weight of sample that has been dried for at least 4 days in a vacuum oven at 60ºC until a constant weight is reached. V is the volume of the cylinder.

X-ray powder diffraction (XRD, 40 kV, 40 mA copper anode X-ray tube) and ATR-FTIR were used to identify amorphous and crystalline phase compositions and phase transitions of tested samples using PDF-4/Minerals 2022 database of International Center for Diffraction Data (ICDD). The Rietveld refinement and quantitative phase analysis was performed with the TOPAS-Academic v7 software. The background intensity, lattice parameters and grain size of each phase were optimized for best fit between the measured and calculated pattern, while the atomic positions and occupancies were fixed to the values reported in the crystallographic information files (CIF) obtained from ICDD or Pearson's Crystal data.

Prior to mechanical testing, the cylindrical cement samples from the borosilicate tubes (18 mm inner diameter x ~145 mm long) are cut into 18 mm x 36 mm cylinders. Electromechanical Instron System Model 5967 with the 30 kN load capacity and 1.25 cm/min loading rate was used to obtain unconfined compressive strength, Young's modulus, and compressive fracture toughness. Compressive strength is the capacity of a material or a structure to resist or withstand compression. Young's modulus (YM) is used as an indicator of the stiffness of the cement composite. In a previous study, Young's modulus was classified into three categories of stiffness; high stiffness is associated with highly brittle composites (YM>2068 MPa), moderate stiffness provides desirable cement performance (2068 MPa>YM> 690 MPa), and soft composites have a detrimental lack of stiffness (YM<690 MPa) (Pyatina & Sugama 2020). High compressive strength is often linked to a high YM, or high brittleness. Compressive fracture toughness is the resistance of the cement to the propagation of cracks developed at ultimate compressive strength (yield point). Whether or not the cracks that form at the yield point lead to catastrophic failure depends on the fracture toughness. The values for compressive strength, YM, and toughness are calculated using Bluehill Universal software (Massachusetts, USA). Compressive fracture toughness was computed from the area under the stress-strain curve between the beginning and the end of the compression test using the following equation:

$$T = \frac{4A}{\pi d^2 h}$$

where $\boldsymbol{A}$ is the area under the stress-strain curve, $\boldsymbol{d}$ is initial cylinder diameter, and $\boldsymbol{h}$ is initial cylinder height.

Microstructural analysis was performed using JEOL 7600F scanning electron microscope (SEM) image analysis coupled with energy dispersive spectroscopy (EDS). Freshly fractured surfaces were silver coated to minimize sample charging. Secondary electron images were collected and EDS operated at acceleration voltages of 15 or 20 kV.

3. RESULTS AND DISCUSSION

3.1 Mechanical Properties

Water-fillable porosity decreased 2% from 54% porosity following 1 day at 300°C to 52% porosity following 1 day at 400°C (Fig. 2a). Samples exposed to 7 days of scH_2O conditions showed 4% increase in porosity to 54%, equivalent to the porosity observed after 1 day at 300°C.

Across all exposure conditions, the compressive strength of the composites exceeded the minimum acceptable level of 7 MPa, ranging from 12 MPa to 15 MPa (Fig. 2b). Compressive strength of the composite increased with higher temperature and longer exposure duration (Fig. 2a). Compressive strength increased 13% from 11.9 MPa after exposure to 300°C for 1 day to 13.4 MPa after 400°C 1 day exposure. Increased duration from 1 to 7 days at supercritical conditions resulted in a 14% increase in compressive strength to 15.3 MPa. Compressive strength appears to be unrelated to porosity.

Stiffness increased with exposure to higher temperatures, and for longer duration, but across all exposure conditions the composite remained within the moderate stiffness range. Increasing temperature from 300°C to 400°C increased stiffness by 74%, from 757 MPa to 1320 MPa. And a subsequent 9% increase in stiffness to 1439 MPa was observed by increasing exposure duration from 1 day at scH_2O to 7 days at scH_2O.

Compressive fracture toughness increased with exposure to higher temperatures and for longer durations (Fig. 2d). Toughness increased 41% from 0.37 N*mm/mm3 after a day at 300°C to 0.52 N*mm/mm3 after 1 day at 400°C. Longer exposure at supercritical conditions further increased toughness by 50% to 0.78 N*mm/mm3 after 7 days scH_2O.

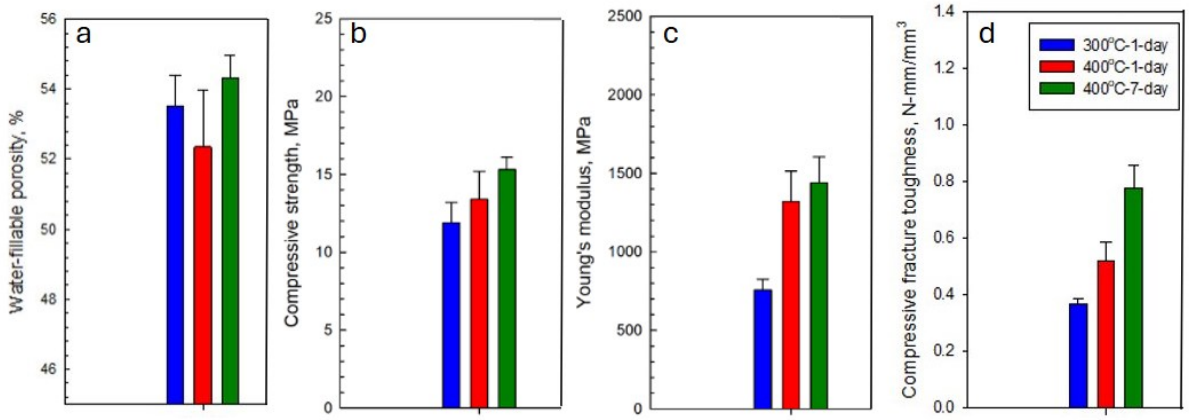

Figure 2. a) water-fillable porosity, b) compressive strength, c) Young's modulus, d) compressive fracture toughness for cement composite exposed to 300°C for 1 day (blue) and 400°C for 1 day (red) and 7 days (green).

Table 1. Mechanical properties of composite over different exposure conditions

	300°C 1 day	400°C 1 day	400°C 7 days	Δ 300°C to 400°C 1 day (%)	Δ 400°C 1 day to 7 days (%)
Compressive strength (MPa)	11.9±1.3	13.4±1.8	15.3±0.8	12.6	14.2
Young's modulus (MPa)	757±68.4	1320±193	1439±165	74.4	9.0
Toughness (N*mm/mm^3)	0.37±0.02	0.52±0.07	0.78±0.08	40.5	50.0

3.2 Phase Compositions

X-ray diffraction was used to identify the phase composition and volume fraction of the resulting phases in each sample (reported in parentheses below and Table 2) (Fig. 3). After 1 day exposure at 300°C, boehmite was the major crystalline reaction product identified (49.2 ± 0.3% volume), along with two minor zeolite phases analcime (11.25 ± 0.2%) and Na-P2 zeolite [$Na_4Al_4Si_{12}O_{32}(H_2O)_{14}$] (0.75 ± 0.1%). Unreacted silica (38.8 ± 0.3%) remained. No crystalline gibbsite was identified.

Following 1 day exposure at scH_2O conditions, Na-P2 zeolite disappeared and a 1% increase in analcime was observed (12.12 ± 0.2%). Boehmite remained the major phase, increasing by 1% (50.4 ± 0.3%), paired with a 1% decrease in silica (37.5 ± 0.3%). After 7 days exposure to supercritical conditions, analcime disappeared and a large percentage of paragonite [$NaAl_2(Si_3Al)O_{10}(OH)_2$] (27.6 ± 0.6%) developed, paired with an 8% decrease in boehmite (42.2 ± 0.4%), and 7% decrease in silica (30.2 ± 0.4%).

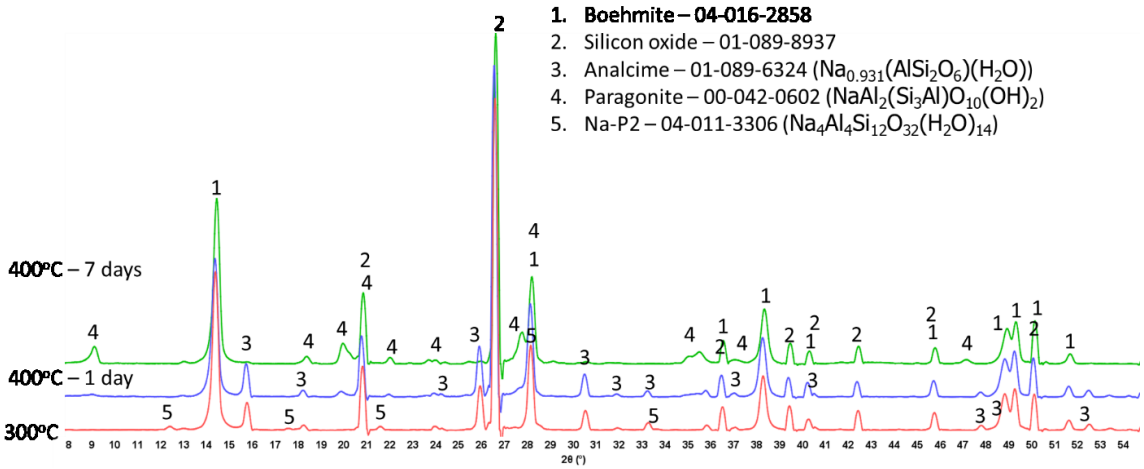

Figure 3. X-ray diffraction patterns of cement composites after autoclaved at 300°C for 1 day (red), and after exposures for 1 day (blue) and 7 days (green) in *sc*H_2O at 400°C.

Table 2. Rietveld calculated volumetric percentage of each phase for different exposure conditions

Exposure conditions	Volume percent of each phase									
	Na-P2	Error	Analcime	Error	Paragonite	Error	Boehmite	Error	Silica	Error
1 day 300°C	0.75	0.1	11.3	0.2	0	0	49.2	0.3	38.8	0.3
1 day 400°C	0	0	12.1	0.2	0	0	50.4	0.3	37.5	0.3
7 days 400°C	0	0	0	0	27.6	0.6	42.2	0.4	30.2	0.4

XRD results are supported by ATR-FTIR. The ATR-FTIR spectra of all samples were collected in the 4000 to 650 cm^{-1} frequency range (Fig. 4). The bands at 3297, 3085, 10654 734 cm^{-1} and the shoulder bands at 1169 and 996 cm^{-1} belong to boehmite. The 3297, 3085, 1169, 1065 and 734 cm^{-1} bands, respectively, were ascribed to $\nu_{as\ O\text{-}H}$, $\nu_{s\ O\text{-}H}$, $\delta_{as\ Al\text{-}O\text{-}H}$, $\delta_{s\ Al\text{-}O\text{-}H}$, in Al-O-H bond and $\nu_{s\ Al\text{-}O}$ in octahedral AlO_6 (Hsiang et al. 2007, Boumaza et al. 2009, Rajaram & Kim 2017). Zeolites including analcime, phillipsite, Na-P2 zeolite and gismondine have bands characteristic of asymmetric stretching vibration of tetrahedral Si-O-T (T is Si and Al) oxygen-bridged bond structure in the 1025 to 998 cm^{-1} range, and symmetric stretching vibration of the same bridge bond in the 794 to 709 cm^{-1} range (Liu et al. 2005, Mozgawa & Król 2011, Chukanov et al. 2018, Jiménez et al. 2021). Because XRD identified two zeolites, analcime and Na-P2, the weak shoulder band at 996 cm^{-1} and band at 734 cm^{-1} belong to the $\nu_{as\ T\text{-}O}$ and $\nu_{s\ T\text{-}O}$, respectively, in the tetrahedral Si-O-T bond structure. The latter band is likely to overlap with octahedral AlO_6 in boehmite. Following exposure to scH_2O for 1 day, the 996 cm^{-1} and 734 cm^{-1} bands increased in intensity corresponding to the increased percentage of zeolite. And after 7 days exposure to scH_2O, a dramatic increase in intensity was observed in the 996 cm^{-1} and 734 cm^{-1} bands due to the formation of paragonite. The peak amplitude for boehmite (1065 cm^{-1}) and zeolite or paragonite (996 cm^{-1}) was calculated after subtracting background intensity (ΔA) and is reported in Table 3. The ratio of boehmite to zeolite or paragonite is calculated for each exposure condition. This ratio starts at 4.14 for 300°C 1 day, decreases to 2.20 after 1 day at 400°C, and further decreases to 1.00 after 7 days at 400°C, indicating that the relative amounts of boehmite to zeolite/paragonite become more equivalent with increased temperature and exposure duration to scH_2O, by a decrease in boehmite, an increase in zeolite/paragonite, or a combination of the two.

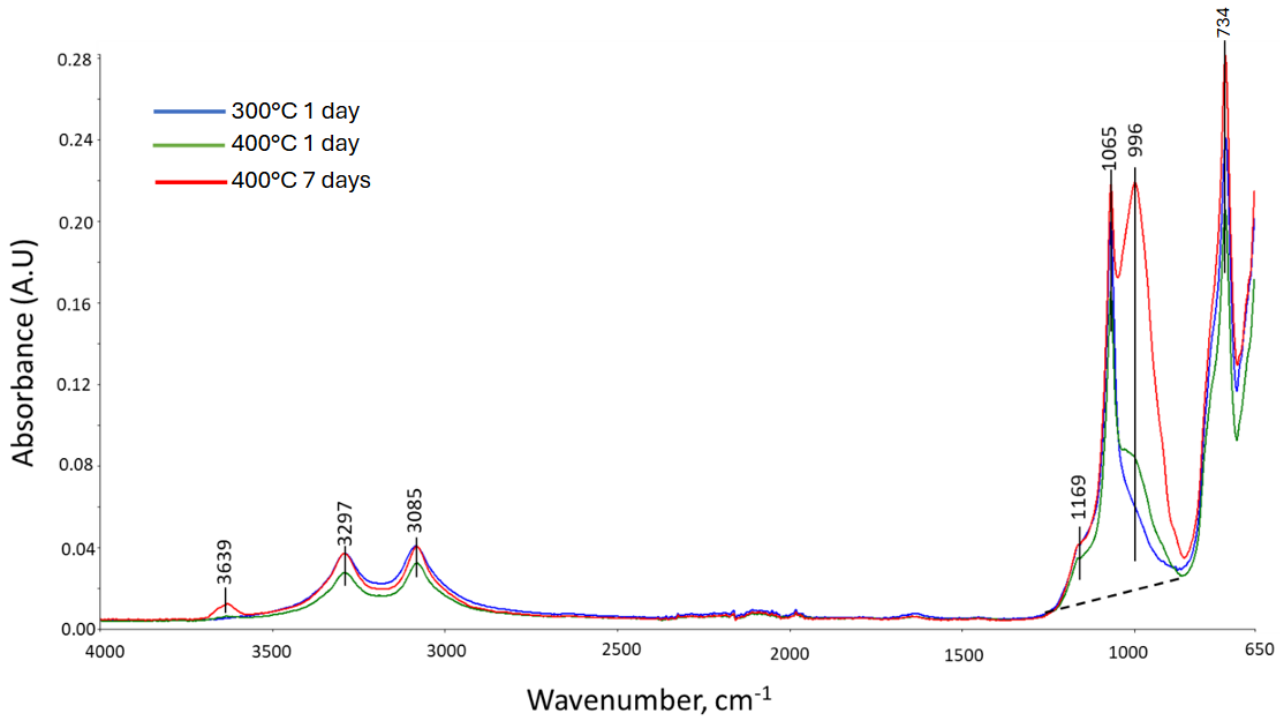

Figure. 4. ATR-FTIR absorption spectra for cement composite exposed to 300°C for 1 day and 400°C for 1 day and 7 days.

Table 3. Absorbance bands height ratios ΔA at 1065 cm^{-1} of boehmite/ ΔA at 996 cm^{-1} of zeolite or paragonite after different curing conditions (Fig. 4)

Exposure conditions	$\Delta A_{1065\ cm-1}$	$\Delta A_{996\ cm-1}$	$\Delta A_{1065}/\Delta A_{996}$
300ºC	0.182	0.044	4.14
400ºC-1 day	0.152	0.069	2.20
400ºC-7 day	0.204	0.205	1.00

3.3 SEM-EDS Microstructure

Scanning electron microscopy (SEM) paired with energy dispersive spectroscopy (EDS) was used to study the microstructural evolution of the samples. After 1 day at 300°C, the matrix of the sample was comprised of plate-like boehmite crystals approximately 3-5 um in diameter (DeSouza et al. 2009) (Fig. 5a, location #1). Large, unreacted quartz crystals are embedded in the boehmite matrix (Fig. 5a, location #2). Following exposure to scH_2O at 400°C for 1 day, a greater amount of analcime is seen among the boehmite matrix. Boehmite crystal size is approximately 5-10 um in diameter. Large unreacted quartz crystals remain surrounded by boehmite and analcime matrix (Fig. 5b).

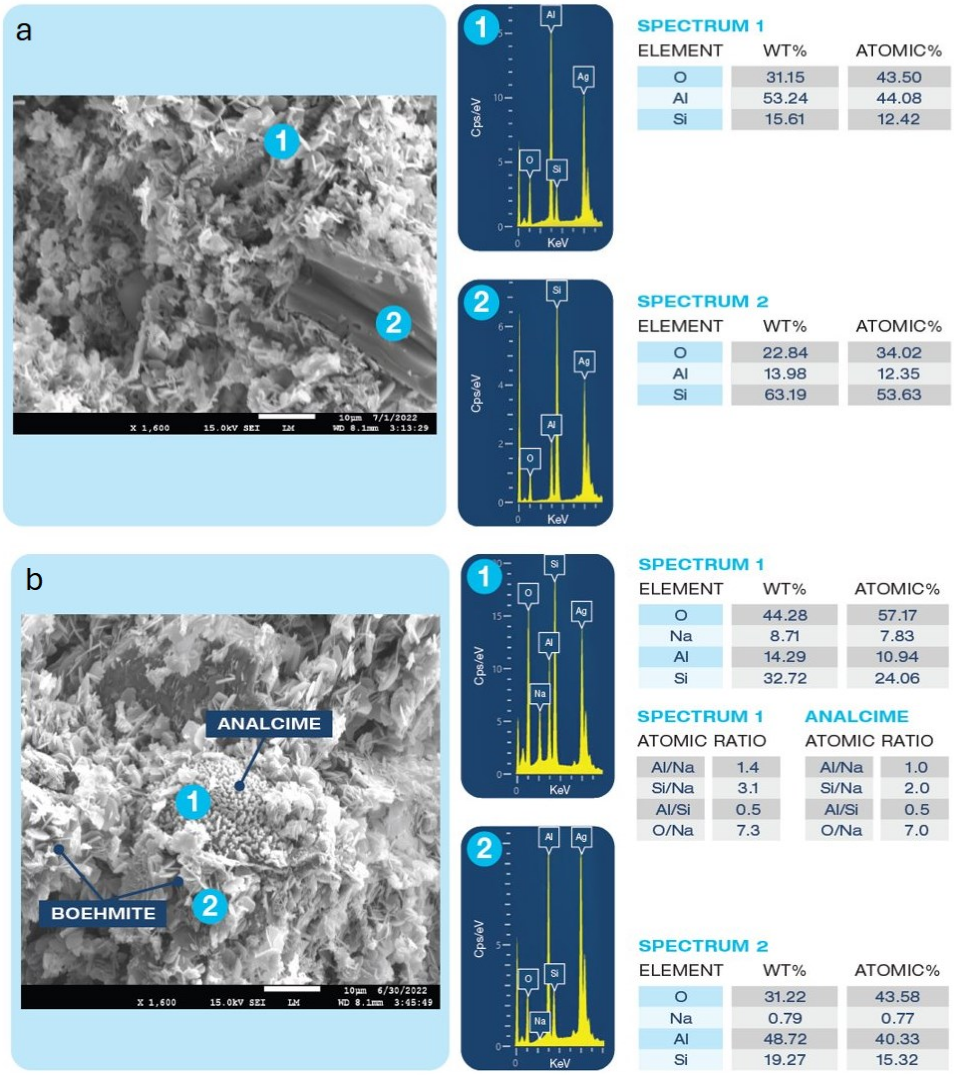

Figure 5. a) Morphology and elemental compositions at two typical locations for 300ºC autoclaved cement. b) Crystalline phase identification in cement after 1 day exposure in scH_2O. Based on atomic ratios crystals at sites #1 and #2 were identified as analcime and boehmite respectively.

3.1 Discussion

The hydrothermal curing of the gibbsite-silica-SMS system resulted in a cementitious composite consisting of boehmite and zeolite (Na-P2 and analcime) matrix surrounding quartz grains, and the later development of paragonite (Fig. 5, Table 2). Compressive strength, YM, and toughness all increased with increased temperature and exposure duration (Fig. 2, Table 1). This coincided with the transformation of Na-P2 to analcime, and ultimately to paragonite (Table 2).

The phase transitions reported suggest the following cement-forming events after the slurry mixing. The starting materials released $Al(OH)_4^-{}_{(aq)}$ from gibbsite, and $SiO_2(OH)_2^{2-}$ anions and Na^+ cations from SMS (Na_2SiO_3) (Yang et al. 2008) at ambient temperature. Before reaching 300°C, the alkali dissolution of gibbsite leads to the hydrothermal synthesis of boehmite. At 300°C, Na-P2 and analcime precipitate as minor phases coexisting with boehmite and quartz as the major phase (Table 2). The phase transition of Na-P2 to analcime upon scH_2O exposure suggests metastable Na-P2 likely transformed to the more stable analcime at higher temperature (Fournier et al. 2017). Extended exposure (7 days) to scH2O saw the development of a significant paragonite [$NaAl_2(AlSi_3O_{10})(OH)_2$] fraction (28%) paired with a disappearance of analcime, 8% decrease in boehmite, and 7% decrease in silica (Table 2). Decreased silica content following 400°C exposure could be explained by increased reactivity of quartz at higher temperatures (Tester et al. 1994). The analcime to paragonite transformation suggests an increase in the $Al^{3+}{}_{(aq)}/3H^+{}_{(aq)}$ ratio (Savage 1986), which can be explained by an influx of Al^{3+} from the degradation of boehmite, and Na^+ must come from the decomposition of analcime. The phase transitions and products of *in-situ* supercritical hydrothermal syntheses described above are summarized in Figure 6.

An improvement in mechanical properties following supercritical exposure coincided with minor changes in phase composition and porosity (Fig. 3, Table 2). Lower porosity is often associated with higher strength (Odler & Rößler 1984, Kumar & Bhattacharjee 2003), so it is possible that the increase in strength observed following 1 day scH2O exposure is related to the 2% decrease in porosity.

The 74% increase in YM from 1 day at 300°C to 1 day at scH_2O suggests a significant increase in composite brittleness. Increased brittleness can be related to the increased crystallinity, as well as lower water content. Amorphous fraction was not quantified in this study, but it is possible that the crystallinity of the composite increased due to accelerated crystallization processes under the supercritical conditions (García-González et al. 2008, Musumeci et al. 2022). It is also possible that analcime influences mechanical properties differently from Na-P2, but no comparative studies between these two zeolites have been done.

Remarkably, toughness, a measure of strength and ductility, continues to increase steadily with increased exposure to scH_2O conditions despite increase of the stiffness. After 1 day at scH_2O, toughness increased 41% compared to the 300°C 1 day sample, and increased another 50% after 7 days exposure to scH_2O. The increase in toughness coincides with the formation of paragonite. Sheet silicates like paragonite are often associated with increased composite ductility (e.g. Shea & Kronenberg 1993), and therefore the 50% increase in toughness observed following 7 days at scH_2O could be related to the development of paragonite. The increase of toughness upon initial exposure to supercritical conditions could be indicative of the formation of undetected nanocrystalline paragonite.

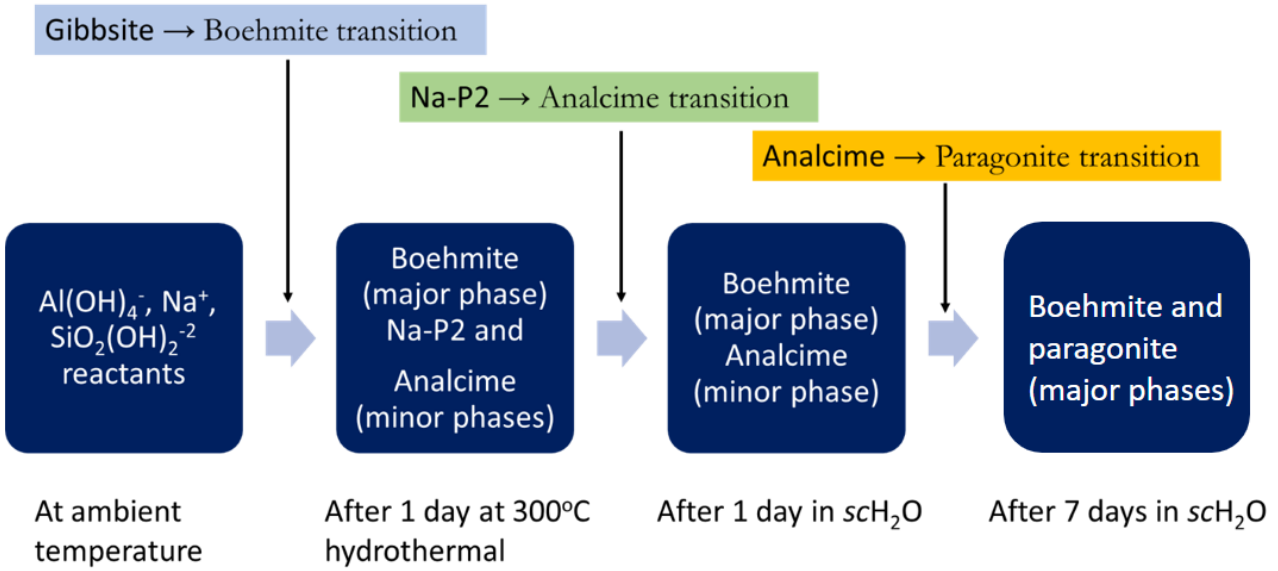

Figure 6. Illustration of the phase transitions and phase compositions in SMS-activated gibbsite cement at hydrothermal temperatures ranging from ambient to 400°C and for up to 7 days of scH_2O exposure.

3. CONCLUSIONS

In this study, an aluminate-based cement system comprised of gibbsite, silica, and the alkaline activator sodium metasilicate was tested for its suitability to be used in supercritical geothermal wells. The composite was cured at 300°C 1 day, and scH_2O for 1 day and 7 days.

The mechanical properties of the composite at each exposure condition were measured, and the composition was determined using TGA-DTG, FTIR, and XRD. Exposure to higher temperatures and for longer durations resulted in higher compressive strength, YM, and ductility, which coincided with the transformation of Na-P2 to analcime upon initial exposure to scH_2O. Longer exposure to scH_2O resulted in the disappearance of all zeolites and the development of a significant fraction of paragonite, which likely contributed to the increased toughness of the composite at supercritical conditions. Overall, the alkali-activated aluminate-based cement demonstrated acceptable mechanical properties for well conditions (minimum compressive strength of 7 GPa, and a moderate brittleness) at each exposure condition.

REFERENCES

Allahdin, O., Wartel, M., Tricot, G., Revel, B., and Boughriet, A.: Hydroxylation and Dealumination of a Metakaolinite-Rich Brick Under Acid Conditions, and Their Influences on Metal Adsorption: One- Andtwo-Dimensional (1H,27Al,23Na,29Si) MAS NMR, and FTIR Studies, Microporous and Mesoporous Materials, 226, (2016), 360–368.

Beddoe, R.E., and Dorner, H.W.: Modelling Acid Attack on Concrete: Part I. The Essential Mechanisms, Cement and Concrete Research, 35, (2005) 2333-2339.

Biczok, I.: Concrete Corrosion and Concrete Protection, Chemical Publishing Company, Inc., New York, NY (1967) pp. 545.

Blankenship, D., Gertler, C., Kamaludeen, M., O'Connor, M., and Porse, S.: Pathways to Commercial Liftoff: Next-Generation Geothermal Power [online] (2024), https://liftoff.energy.gov/next-generation-geothermal-power/.

Boumaza, A., Favaro, L., Lédion, J., Sattonnay, G., Brubach, J.B., Berthet, P., Huntz, A.M., Roy, P., and Tétot, R.: Transition Alumina Phases Induced by Heat Treatment of Boehmite: An X-Ray Diffraction and Infrared Spectroscopy Study, Journal of Solid State Chemistry, 182, (2009), 1171–1176.

Chukanov, N. V., Zubkova, N. V., Meisser, N., Ansermet, S., Weiss, S., Pekov, I. V., Belakovskiy, B., Vozchikova, S.A., Britvin, S.N., and Pushcharovsky, D.: Martinandresite, Ba 2 (Al 4 Si 12 O 32)·10H 2 O, a New Zeolite from Wasenalp, Switzerland, Physics and Chemistry of Minerals, 45, (2018), 511–521.

Cladouhos, T.T., Petty, S., Bonneville, A., Schultz, A., and Sorlie, C.F.: Super Hot EGS and the Newberry Deep Drilling Project, Proceedings, 43rd Workshop on Geothermal Reservoir Engineering, Stanford University, Stanford, CA, (2018).

De Souza Santos, P., Coelho, A.C.V., De Souza Santos, H., and Kiyohara, P.K.: Hydrothermal Synthesis of Well-Crystallised Boehmite Crystals of Various Shapes, Materials Research, 12, (2009), 437–445.

Earnest, C.M., Gann, K., Stong, B. Improved quantification of gibbsite in bauxite ores by thermgravimetric methods (TGA and DTG). Adv. Appl. Chem. Biochem. 1 (2018) 1-17.

Ferraro, J.R., and Manghnani, M.H.: Infrared Absorption Spectra of Sodium Silicate Glasses at High Pressures, Journal of Applied Physics, 43, (1972), 4595–4599.

Fidalgo, A., Ilharco, L.M.: The Defect Structure of Sol-Gel-Derived Silica/Polytetrahydrofuran Hybrid Films by FTIR, Journal of Non-Crystalline Solids, 283, (2001), 144–154.

Fournier, M., Gin, S., Frugier, P., and Mercado-Depierre, S.: Contribution of Zeolite-Seeded Experiments to the Understanding of Resumption of Glass Alteration, npj Materials Degradation, 1, (2017) 17.

Gallus, J.P., Watters, L.T., and Pyle, D.E.: Performance of Oilwell Cementing Compositions in Geothermal Wells, Society of Petroleum Engineers Journal, 4, (1979), 233-241.

García-González, C.A., el Grough, N., Hidalgo, A., Fraile, J., López-Periago, A.M., Andrade, C., and Domingo, C.: New Insights on the Use of Supercritical Carbon Dioxide for the Accelerated Carbonation of Cement Pastes, Journal of Supercritical Fluids, 43, (2008), 500-509.

Gill, S.K., Pyatina, T., andSugama, T.: Thermal Shock-Resistant Cement, GRC Transactions, 36, (2012) 445-451.

Gong, X., Nie, Z., Qian, M., Liu, J., Pederson, L.A., Hobbs, D.T., and McDuffie, N.G.: Gibbsite to Boehmite Transformation in Strongly Caustic and Nitrate Environments., Ind. Eng. Chem. Res., 42, (2003), 2163-2170.

Hsiang, H.I., Liang, M.T., Huang, H.C., Yen, F.S.: Preparation of Superhydrophobic Boehmite and Anatase Nanocomposite Coating Films, Materials Research Bulletin, 42, (2007) 420–427.

Husung, R.D., and Doremus, R.H.: The Infrared Transmission Spectra of Four Silicate Glasses Before and After Exposure to Water, Journal of Materials Research, 5, (1990) 2209–2217.

Innocenzi, P., Falcaro, P., Grosso, D., and Babonneau, F.: Order-Disorder Transitions and Evolution of Silica Structure in Self-Assembled Mesostructured Silica Films Studied through FTIR Spectroscopy. Journal of Physical Chemistry B, 107, (2003) 4711-4717.

Jiménez, A., Misol, A., Morato, Á., Rives, V., Vicente, M.A., and Gil, A.: Synthesis of Pollucite and Analcime Zeolites by Recovering Aluminum from a Saline Slag, Journal of Cleaner Production, 297, (2021) 126667.

Kruszewski, M., and Wittig, V.: Review of Failure Modes in Supercritical Geothermal Drilling Projects, Geothermal Energy, 6, (2018), doi: 10.1186/s40517-018-0113-4.

Kumar, R., and Bhattacharjee, B.: Porosity, Pore Size Distribution and In Situ Strength of Concrete, Cement and Concrete Research, 33, (2003) 155-164.

Li, B., Li, H., Zhang, X., Fan, P., Liu, L., Li, B., Dong, W., Zhao, B.: Calcined Sodium Silicate as an Efficient and Benign Heterogeneous Catalyst for the Transesterification of Natural Lecithin to L-α-Glycerophosphocholine, Green Processing and Synthesis, 8, (2019), 78-84.

Liu, B.S., Tang, D.C., and Au, C.T.: Fabrication of Analcime Zeolite Fibers by Hydrothermal Synthesis, Microporous and Mesoporous Materials, 86, (2005), 106–111.

Mozgawa, W., and Król, M.: FT-IR Studies of Zeolites from Different Structural Groups Synthesis and Structural Studies of Zeolite Membranes on Geopolimeric Supports View Project FT-IR Studies of Zeolites from Different Structural Groups, Chemik, 65, (2011), 667-674.

Musumeci, V., Camacho, P.S., Xu, K., Monteiro, P.J.M., Dolado, J.S., and Aymonier, C.: Sub- and Supercritical Hydrothermal Route for the Synthesis of Xonotlite Nanofibers for Application to Green Concrete Materials, Journal of Supercritical Fluids, 184, (2022), 105583.

Odler, I., and Rossler, M. Investigations on the Relationship Between Porosity, Structure, and Strength of Hydrated Portland Cement Pastes. II. Effect of Pore Structure and of Degree of Hydration, Cement and Concrete Research, 15, (1985), 401-410.

Petty, S., Cladouhos, T., Watz, J., and Garrison, G.: Technology Needs for SuperHot EGS Development, Proceedings, 45th Workshop on Geothermal Reservoir Engineering, Stanford University, Stanford, CA (2020).

Pyatina, T., and Sugama, T.: Acid Resistance of Calcium Aluminate Cement-Fly Ash F Blends, Advances in Cement Research, 28, (2016) 433-457.

Pyatina, T., and Sugama, T.: Cements with Supplementary Cementitious Materials for High-Temperature Geothermal Wells, Geothermics, 86, (2020), 101840.

Pyatina, T., and Sugama, T.: Aluminum-Rich Cements for High Temperature Geothermal Wells, Proceedings, 49th Workshop on Geothermal Reservoir Engineering, Stanford University, Stanford, CA (2024).

Rajaram, K., Kim, J.: Surfactant Assisted Fabrication of Different Nanostructures of Boehmite by Hydrothermal Process, International Journal of Applied Engineering Research, 12, (2017) 2781–2787.

Ramasamy, V., and Suresh, G.: Mineral Characterization and Crystalline Nature of Quartz in Ponnaiyar River Sediments, Tamilnadu, India, Journal of Scientific Research, 4, (2009), 103–107.

Reinsch, T., Dobson, P., Asanuma, H., Huenges, E., Poletto, F., and Sanjuan, B.: Utilizing Supercritical Geothermal Systems: A Review of Past Ventures and Ongoing Research Activities, Geothermal Energy, 5, (2017), 1-25.

Savage, D. Granite-Water Interactions at 100C, 50 MPa: An Experimental Study, Chemical Geology, 54, (1986) 81-95.

Schroeder, P.A.: Infrared Spectroscopy in Clay Science. In *CMS Workshop Lectures, Vol. 11, Teaching Clay Science*; Rule, A., Guggenheim, S., Eds.; The Clay Mineral Society: Aurora, CO, 2002; pp. 181–206.

Shea, Jr., W.T., and Kronenberg, A.K.: Strength and Anisotropy of Foliated Rocks with Varied Mica Contents, Journal of Structural Geology, 15, (1993), 1097-1121.

Sugama, T., and Carciello, N.R.: Carbonation of Hydrothermally Treated Phosphate-Bonded Calcium Aluminate Cements, Cement and Concrete Research, 22, (1992), 783-792.

Sugama, T., and Carciello, N.R.: Carbonation of Calcium Phosphate Cements After Long-Term Exposure to Na_2CO_3-Laden Water at 250°C, Cement and Concrete Research, 23, (1993), 1409-1417.

Sugama, T., and Carciello, N.R.: Sodium Phosphate-Derived Calcium Phosphate Cements, Cement and Concrete Research, 25, (1995), 91-101.

Sugama, T., and Pyatina, T.: Self-Healing, Re-Adhering, and Corrosion-Mitigating Inorganic Cement Composites for Geothermal Wells at 270°-300°C, BNL-2019-IR, (2019), doi:10.2172/1501577.

Suryanarayana, P.V., Krishnamurthy, R.V., and Bour, D.: Bridging the Gaps: A Survey of Methods, Challenges, and Pathways Forward for Superhot Rock Well Design and Construction. Clean Air Task Force. pp. 61. Accessed 2025. https://www.catf.us/superhot-rock/bridging-gaps/

Tarte, P.: Infra-Red Spectra of Inorganic Aluminates and Characteristic Vibrational Frequencies of AlO_4 Tetrahedra and AlO_6 Octahedra, Spectrochimica Acta Part A: Molecular Spectroscopy, 23, (1967), 2127–2143.

Tester, J.W., Worley, W.G., Robinson, B.A., Grigsby, C.O., and Feerer, J.L.: Correlating Quartz Dissolution Kinetics in Pure Water from 25 to 625C, Geochimica et Cosmochimica Acta, 58, (1994), 2407-2420.

Xyla, A.G., and Koutsoukos, P.G., Quantitative Analysis of Calcium Carbonate Polymorphs by Infrared Spectroscopy. J. Chem. Soc., Faraday Trans. 1, 85, (1989) 3165–3172.

Yang, X., Roonasi, P., and Holmgren, A.: A Study of Sodium Silicate in Aqueous Solution and Sorbed by Synthetic Magnetite Using in Situ ATR-FTIR Spectroscopy. Journal of Colloid and Interface Science, 328, (2008), 41–47.

Ylmen, R., and Jaglid, U.: Carbonation of Portland Cement Studied by Diffuse Reflection Fourier Transform Infrared Spectroscopy, Int J Concr Struct Mater, 7, (2013), 119–125.

Zhang, X., Cui, W., Hu, J.H., Wang, H.-W., Prange, M.P., Wan, C., Jaegers, N.R., Zong, M., Zhang, H., Pearce, C.I., Li, P., Wang, Z., Clark, S.B., and Rosso, K.M.: Transformation of Gibbsite to Boehmite in Caustic Aqueous Solution at Hydrothermal Conditions, Cryst. Growth Des., 19, (2019), 5557-5567.